How to cite: *Angew. Chem. Int. Ed.* **2023**, *62*, e202305695
doi.org/10.1002/anie.202305695

VIP **Redox Flow Batteries** *Very Important Paper*

A Nitrogen Battery Electrode involving Eight-Electron Transfer per Nitrogen for Energy Storage

Haifeng Jiang, Gao-Feng Chen, Guangtong Hai, Wei Wang, Zhenxing Liang, Liang-Xin Ding, Yifei Yuan, Jun Lu, Markus Antonietti,* and Haihui Wang**

Abstract: Redox flow batteries have been discussed as scalable and simple stationary energy storage devices. However, currently developed systems encounter less competitive energy density and high costs, restricting their wider application. There is a lack of appropriate redox chemistry, preferably based on active materials that are abundant in nature and show high solubility in aqueous electrolytes. A nitrogen-centered redox cycle operating between the limiting species ammonia and nitrate via an eight-electron redox reaction stayed practically unnoticed, albeit its ubiquity in biological processes. Ammonia or nitrate are world-scale chemicals with high aqueous solubility, and are then comparably safe. We demonstrate here the successful implementation of such a nitrogen-based redox cycle between ammonia and nitrate with eight-electron transfer as a catholyte for Zn-based flow batteries, which continuously worked for 12.9 days with 930 charging-discharging cycles. A very competitive energy density of 577 Wh L^{-1} can be reached, which is well above most reported flow batteries (e.g. 8 times the standard Zn-bromide battery), demonstrating that the nitrogen cycle with eight-electron transfer can offer promising cathodic redox chemistry for safe, affordable, and scalable high-energy-density storage devices.

Redox flow batteries (RFBs) are promising candidates for stationary energy storage devices for modern grids based on intermittent green energy generation.[1] RFBs are unique since electrolyte and electrode are spatially separated, which has the advantages of safety, simplifies scalability and independent tuning of the energy and power output.[2] Besides liquid-liquid RFBs, hybrid-flow batteries combining a multivalent metal (such as Zn, Mg and Al) anode with a redox-active catholyte have attained attention.[3] Until very recently, reported research on electroactive species of the catholyte was rather limited and has been focused mostly on transition metal redox species, halogen, or aqueous soluble organic redox materials.[4] As a mature technology and after a few decades of development, the zinc-bromine RFB has become the reference flow battery for scaled demonstrators, but its industrialization is still hindered by the relatively high cost and low energy density, regarding the low natural abundance of bromine, its high mass, and the low solubility of active materials in the catholyte, respectively.[5] According to the energy density calculation equation ($E = NCFV/n$, where N is the number of electrons transferred in the redox reaction, C is the concentration of active redox species, F is the Faraday constant, V is the voltage, and n is the number of electrolyte volumes contributing to redox reactions), maximizing N, C and V while minimizing n is beneficial to enhance E.[6]

Until recently, efforts were devoted to exploring novel electroactive materials with high aqueous solubility, yet little attention has been paid to the number of electrons transferred in the redox reaction.[7] Most of the reported cathodic active species such as VO_2^+/VO^{2+}, I^-/I_3^-, I^-/I_2, Br^-/Br_2, $Fe(CN)_6^{4-}/Fe(CN)_6^{3-}$, $Ni(OH)_2/NiOOH$, etc. experience single- or two-electron redox reactions while four electrons are involved in the case of Pb redox, (e.g., PbO_2/Pb) (Figure 1a).[8] It is obvious that a higher electron transfer number per unit of active material will significantly reduce the concentration of active material used, thus reducing the costs and increasing the energy density. In this regard, Zn-

[*] H. Jiang, Dr. G. Hai, Prof. H. Wang
Beijing Key Laboratory for Membrane Materials and Engineering, Department of Chemical Engineering, Tsinghua University
Beijing 100084 (China)
E-mail: cehhwang@tsinghua.edu.cn

H. Jiang, Dr. G.-F. Chen, Prof. Z. Liang, Prof. L.-X. Ding
School of Chemistry and Chemical Engineering, South China University of Technology
Guangzhou 510640 (China)
E-mail: gaofeng.chen@mpikg.mpg.de

Dr. G.-F. Chen, Prof. M. Antonietti
Department of Colloid Chemistry, Max-Planck Institute of Colloids and Interfaces, Research Campus Golm
Am Mühlenberg 1, 14476 Potsdam (Germany)
E-mail: Markus.Antonietti@mpikg.mpg.de

Prof. J. Lu
College of Chemical and Biological Engineering, Zhejiang University
Hangzhou, Zhejiang 310027 (China)

W. Wang, Prof. Y. Yuan
College of Chemistry and Materials Engineering, Wenzhou University
Wenzhou 325035 (China)

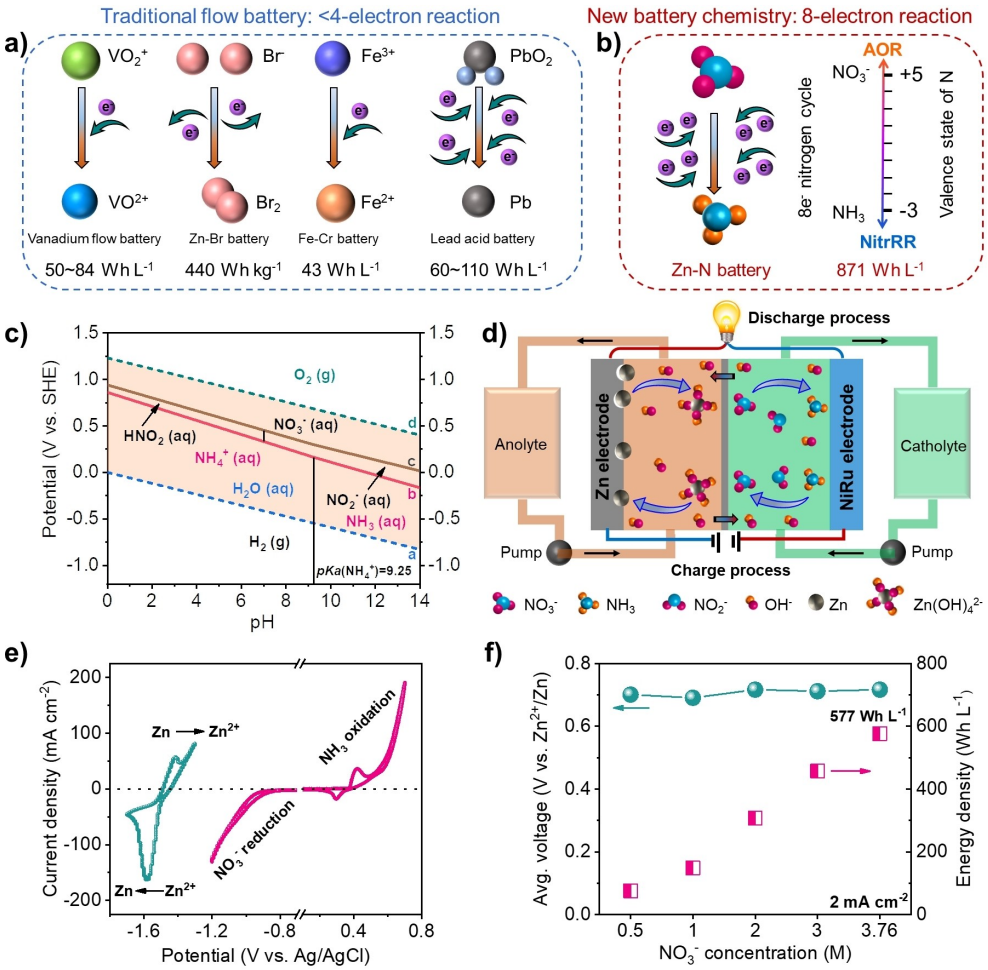

Figure 1. Schematic illustration and performance indicators of hybrid Zn–Zn^{2+}//NO_3^-–NH_3 flow battery. a) Representative traditional flow battery and corresponding theoretical energy density (See the Table S1 for detailed data and references). b) Eight-electron nitrogen cycle between NO_3^- and NH_3 and its high theoretical energy density. c) Partial Pourbaix diagrams of NO_x^-–NH_3 ($x=2$, 3) system. Dotted lines *a* and *d* correspond to the region of H_2 evolution and O_2 evolution, respectively by water splitting. Solid lines *b* and *c* represent the redox couple of NO_2^-/NH_3 and NO_3^-/NO_2^-, respectively. The potential-pH predominance diagram (Pourbaix) elucidates that the transform between NO_x^- ($x=2$, 3) and NH_4^+ (NH_3) is thermodynamically feasible under appropriate redox conditions. d) Schematic illustration of hybrid Zn–Zn^{2+}//NO_3^-–NH_3 flow battery. e) CV curves of Ti foil electrode (1×2 cm^2) and NiRu electrode recorded in 50 mL 3 M KOH/0.5 M Zn^{2+} and 3 M KOH/0.5 M NO_3^-/0.5 M NH_3 electrolyte, respectively, at a scan rate of 5 mV s^{-1}. f) Average discharging voltage at different NO_3^- concentrations and corresponding calculated energy density based on the assumption that when all NO_3^- is converted to NH_3.

air batteries that integrate a zinc metal anode and a four-electron redox reaction oxygen cathode based on dioxygen (i.e. 2 electrons per oxygen) are worth mentioning.[9] However, the slow kinetics of such a gas-solid-liquid three-phase reaction and carbonate formation when getting in touch with CO_2 in air limit practicality.[10] Another reported competitor is a H_2/$NaBrO_3$ flow battery with a six-electron transfer process, but this faces the disadvantages of scarcity of Br and its high mass.[11]

Nitrogen redox chemistry is ubiquitous in the environment and critical to all life, but its applications in electrochemical energy storage are poorly understood. In water, nitrogen is commonly found as nitrate (NO_3^-), nitrite (NO_2^-) or ammonium ion (NH_4^+) with oxidation states of +V, +III, and −III, respectively. At the standard potential of 0.88 V versus normal hydrogen electrode (vs. NHE, pH 0),[12] the transformation between NO_3^- and NH_4^+ involves an eight-electron reaction (that is, one electron per 7.7 mass units). This could set the base for a more than competitive active material formulated as a catholyte. For example, such a zinc-nitrogen hybrid flow battery (Zn–N battery, ZNB) has an ideal theoretical energy density of 871 Wh L^{-1} at the solubility limit of KNO_3 in the water (38 g/100 mL, 25 °C), which is much higher than that of the lead battery, vanadium redox battery, Zn–Br_2 battery, Zn–MnO_2, and many others (see Figure 1b). Besides, in terms of the abundance of the active materials, the NO_3^- is a mass chemical, particularly abundant, and can even be retrieved from wastewater by ion exchange in the conventional denitrification process.[13] Very recently, NO_3^- pollutant solutions were used as promising alternatives to dissolved nitrogen and were demonstrated to be easily electro-

converted to valued-added NH_3 (NitrRR) under ambient conditions due to the low dissociation energy of the –N=O bond (204 kJ mol^{-1}) and high absolute solubility of NO_3^- in water.[14] Especially combining the NitrRR-based cathode with metal anode as a galvanic cell for not only NH_3 synthesis but electricity production is highly attractive.[15] NH_3, on the other hand, is synthesized from N_2 in over 200 million tons per year by the traditional Haber-Bosch process and is extensively used in fertilizer production.[15b,16] The conversion of NH_3 to nitric acid in the industry is operated by the Ostwald process with noble metals (Pt, Rh) as catalysis under conditions of high temperatures (800–930 °C) and pressures (4–15 bar).[17] Although the electrochemical oxidation reaction of NH_3 to NO_3^- with high selectivity has not been reported, the ammonia oxidation reaction (AOR) to NO_3^- is thermodynamically favored with appropriate potentials under all pH conditions, as proved by the standard equilibrium potentials in dependence of pH (Pourbaix diagram, Figure 1c).

On the basis of all that knowledge, here an alkaline Zn-based RFB ($Zn–Zn^{2+}//NO_3^-–NH_3$) is chosen to demonstrate the feasibility of an aqueous nitrogen cycling process for the cathode, a battery which offers a theoretical operating voltage of 1.08 V [Figure 1d, Eq. (1)–(3) (vs. NHE, pH 14)] and the discussed high energy density. Specifically, a divided cell separated by a Nafion membrane is constructed with a Zn metal and a NiRu catalyst-based cathode. The anolyte is composed of 3.0 M KOH solution mixed with saturated $Zn(OH)_4^{2-}$ while the catholyte consists of 0.5 M NO_3^- and saturated NH_3 alkaline solution (3.0 M KOH), both of which are pumped through two half-cells, respectively. We clearly mention that the choice of Nafion for an alkaline cell is suboptimal and accounts for some of the losses reported below, but the choice was done based on availability.

$$\text{Cathode}: \ NO_3^- + 6H_2O + 8e^- \rightarrow NH_3 + 9OH^- \qquad E^o = -0.12\ V \tag{1}$$

$$\text{Anode}: \ 4Zn + 16OH^- \rightarrow 4Zn(OH)_4^{2-} + 8e^- \qquad E^o = -1.20\ V \tag{2}$$

$$\text{Overall}: \ 4Zn + NO_3^- + 6H_2O + 7OH^- \leftrightarrow 4Zn(OH)_4^{2-} + NH_3 \qquad E^o = 1.08\ V \tag{3}$$

Electrocatalysts enabling high activity and selectivity for NitrRR and AOR are a prerequisite for the cathodic half-cell. In this regard, recent research work has provided insights into the Cu-, Ni-, Co-, and Ru-based electrocatalysts to realize a full eight-electron NitrRR process.[18] For the AOR process, we tried to screen catalysts and found that Ni-based materials show high catalytic activity and selectivity but unfortunately poor stability when exposed to NH_3 with a high concentration. Accordingly, a unique NiRu ball-flower structure was designed, where a Ru "pedal armor" protects the catalyst against NH_3 erosion and promotes NitrRR catalysis, while the Ni stamen shows outstanding catalytic activity towards the AOR. In addition to a pair of small redox peaks at ≈0.4 V vs. Ag/AgCl attributed to Ni^{II}/Ni^{III} redox reaction,[19] the cyclic voltammogram (CV) curve collected in a three-electrode system shows one pair of distinct redox peaks, demonstrating the designed NiRu ball-flower catalyst is quite active in catalyzing the forward and backward transformation of the NO_3^-/NH_3 redox couple (Figure 1e). When the catalyst cathode and zinc anode are assembled, the battery delivers a practical discharging voltage of 0.72 V at 2 mA cm^{-2}, which stands for an energy density of 577 Wh L^{-1} (Figure 1f). This is 66.2 % of the theoretical value and the losses are mostly attributed to the voltage drop sourced from the imperfect engineering, but as a proof-of-principle, it still much higher than most reported battery systems, such as 35–45 Wh L^{-1} for lead battery, ≈65 Wh L^{-1} for $Zn–Br_2$ battery, and 25 Wh L^{-1} for vanadium flow battery (Figure 2d).[5,8g,20]

The discharging capability and charging behavior of $Zn–Zn^{2+}//NO_3^-–NH_3$ battery was initially explored in a non-flow, stationary cell. The battery can maintain the voltage level across the entire NO_3^- concentration range (Figure 1f), and we took 0.5 M NO_3^- as a model concentration to further analyze the battery behavior. In a discharging process, the battery shows an open-circuit potential (OCP) of 1.39 V vs. Zn/Zn^{2+} by the electrochemical workstation test (Figure 2a), which is consistent with the result of the multimeter test (Inset of Figure 2a and Figure S1). The higher-than-theoretical OCP is ascribed to the reduction of few metal oxidized species.[19a] The conversion of NO_3^- to NH_3 in the catholyte is paired with the oxidation of Zn at the anode (Figure S2). Two batteries in series can power an electronic calculator working over 50 hours (Figure S3), indicating the practicality of our very small $Zn–Zn^{2+}//NO_3^-–NH_3$ battery. The highest capacitive contribution (CC) of 97.1 % for NH_3 production can be obtained at a high current density of 50 mA cm^{-2} after a 2-hour discharging process, corresponding to an NH_3 production of 7.7 mg mg$_{cat}^{-1}$ (Figures S4–6). The discharge voltage shows no obvious fading after running over 35 hours at 2 mA cm^{-2} and maintains at around 0.7 V (Figure S5e). With increasing discharge time at 20 mA cm^{-2}, the NH_3 content in the electrolyte increases correspondingly. After 50-hour of discharge, 0.2 g NH_4Cl salt (identified by the XRD pattern) can be collected (Figure S7), corresponding to an average CC of 92.7 % (Figure 2b and Table S2). A good rate performance was also achieved (Figure 2c). At 0.1 mA cm^{-2}, the discharge voltage can reach 0.92 V. The voltage recovers to 0.78 V at 0.5 mA cm^{-2} (initial value is 0.83 V) after operation at a high discharge current density of 10 mA cm^{-2}.

In a charging process, NO_x^- ($x = 2, 3$) was found in the saturated NH_3 alkaline electrolyte, implying the oxidation of NH_3 into NO_x^-. The highest CC of 98.1 % was obtained at 5 mA cm^{-2} for NiRu electrode-based battery after 2-hour charging (Figures S8–10), and a CC of 93.3 % was maintained even at a high current density of 20 mA cm^{-2}. Coulombic Efficiency is also a key performance indicator for rechargeable batteries. More than 90 % Coulombic efficiency can be found at the current density exceeding 5 mA cm^{-2} (Figures 2e and S5b), which is comparable with reported battery systems.[21] At a current density of over 30 mA cm^{-2}, the Coulombic efficiency begins to become lower, ascribed to the occurrence of the parasitic oxygen

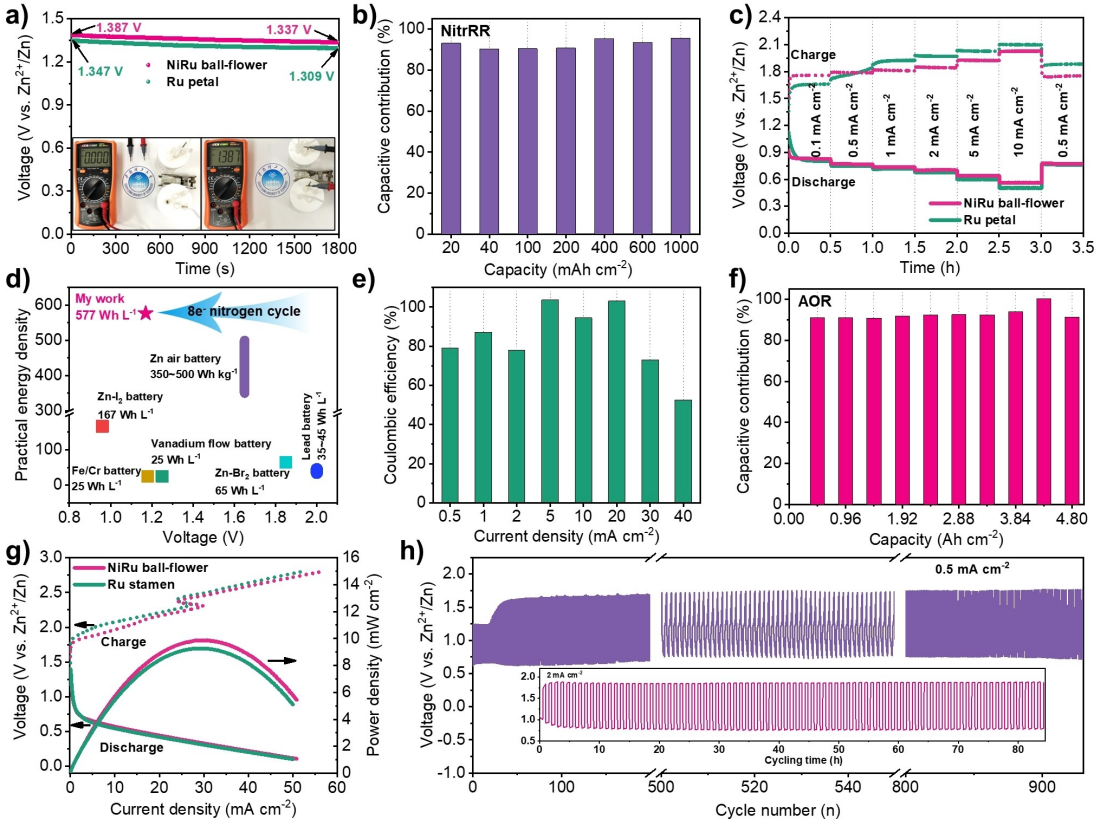

Figure 2. Performance of the rechargeable Zn–Zn^{2+}//NO_3^-–NH_3 battery. a) Open-circuit voltage for Zn–Zn^{2+}//NO_3^-–NH_3 battery when using NiRu ball-flower and pure Ru electrodes for the nitrogen cycle electrocatalysis (Inset: The open circuit voltage of the battery was recorded with a multimeter in the case of disconnection or connection). b) Capacitive contribution during the 50-hour discharging process at 20 mA cm^{-2} (Capacity here is equal to time multiply current density). c) Charge-discharge curves at various current densities from 0.1 mA cm^{-2} to 10 mA cm^{-2}. d) Practical energy density of the Zn–Zn^{2+}//NO_3^-–NH_3 hybrid battery compared with that of several kinds of representative batteries (See the practical energy density from Table S5). e) Coulombic efficiency calculated from charge-discharge product (NO_2^- and NH_3 for discharge process, and NO_2^- and NO_3^- for discharge process). f) Capacitive contribution during 240-hour charging process at 20 mA cm^{-2} (The calculated capacity method is the same as discharging process). g) Charge-discharge polarization curves of NiRu- and pure Ru-electrode based batteries and the resultant power density form the discharge polarization curves. h) Long-term charge and discharge cycles of the Zn–Zn^{2+}//NO_3^-–NH_3 flow battery at 0.5 mA cm^{-2} (Inset of (h): Long-term charge and discharge cycles of Zn–Zn^{2+}//NO_3^-–NH_3 hybrid battery in H-type cell).

evolution reaction (OER) during the charging process. Zn metal deposition on the anode surface was observed after 2-hour charging at 5 mA cm^{-2} and was confirmed by the XRD, SEM and EDS (see detailed discussions in Figures S11–14). The rate performance for charging was also explored (Figure 2c). The loading voltage (1.76 V) at 0.5 mA cm^{-2} can return to the initial value of 1.78 V after charging at a high current density of 10 mA cm^{-2}. The charge-discharge voltage gap at 0.1 mA cm^{-2} is 0.92 V and can be attributed to the overpotential of AOR and NitrRR. In addition, the voltage efficiency of the Zn–N battery was calculated based on charge–discharge curves at various current densities (Table S3). A high voltage efficiency of 47.50 % can be achieved at 0.1 mA cm^{-2}.

For a short-term charging process, nearly half of the oxidation product is NO_2^- (Figure S9a). The full eight-electron transfer process consecutively dominates when the reaction time is longer. As shown in Figures 2f and S15, Table S4, NH_3 finally converts to NO_3^- after 10 days of charge reaction at 20 mA cm^{-2}, and the NO_3^- content linearly increases during that period with a concentration in electrolyte reaching 0.4 mol L^{-1}. The corresponding CC for NO_3^- formation is over 90 % after a 10-day charging process, which explicates the charge capacity of the battery to use the full eight-electron-transfer process. In addition, the discharging polarization curve shows the highest power density of 10.0 mW cm^{-2} (Figure 2g), which is superior to that of recently reported Zn–NO_3^- primary batteries.[15a,22]

The long-term charge-discharge ability of the hybrid Zn–Zn^{2+}//NO_3^-–NH_3 battery was evaluated in an H-type cell and a flow cell (Figures 2h, S16 and S17). For the flow cell, the catholyte and anolyte were stored in two external Teflon fluid reservoirs, respectively, and were cycled by peristaltic pumps (Figure S17). The flow battery was repeatedly charged and discharged at 0.5 mA cm^{-2} for 930 cycles with 20 min per cycle period (12.9 days). After initial activation through the first 35 cycles, the battery showed a slight increase in the loading voltage from 1.58 V in the 35th cycle to 1.72 V in the 500th cycle and finally to 1.76 V in the 930th cycle while the discharge voltage around

0.70 V (Figure 2h), indicating the hybrid Zn–Zn^{2+}/ /NO_3^-–NH_3 RFB is capable of being recharged and has excellent cycle stability of the catalyst. The increasing loading voltage is a known weakness of the zinc anode and can mostly be attributed to this side.

For local monitoring of catalytic mechanism and stability, the material structure and catalytic activity of the NiRu catalyst were further studied in a three-electrode system in detail. The linear sweep voltammetry (LSV) curves show the apparent current density of NO_3^- reduction and NH_3 oxidation reactions. Especially, a current density of 1 A cm^{-2} was reached at comparably low potentials of −0.06 V for NO_3^- reduction reaction (Figure 3a), superior to the previous work.[15a,18d,22a,23] The current density of NO_3^- reduction is similar to that of NO_2^- reduction while the current density of NH_3 oxidation reaction is lower than that of NO_2^- oxidation reaction, indicating the activity of catalyst for NH_3 oxidation to NO_2^- is relatively limited compared to NO_2^- oxidation to NO_3^-. We then sought to quantify the nitrate/nitrite electrosynthesis from AOR in a 1 M KOH solution containing 0.5 M NH_3 and at a series of potentials with a reaction time of two hours (Figure S18). The total Faradaic efficiency (FE) of the NiRu catalyst for NO_x^- ($x=2$, 3) production gradually declines with a positive shift of applied potentials and reached its highest value of 91.02 % at 1.3 V vs. RHE (Figures 3b and S19–S23).

To support the concept of a reversible redox loop of NH_3 and NO_x^-($x=2$, 3), the NitrRR was also studied by employing the NiRu ball-flower catalyst in 1 M KOH solution containing 0.5 M NO_3^- (Figures S24–S29). High FE values of over 93.6 % for the reduction of NO_3^- to NH_3 were observed at potentials ranging from −0.6 V to 0.2 V vs. RHE (Figure 3c). This demonstrates that the side reactions producing hydrogen or dinitrogen products are much-suppressed during NitrRR processes.[24] On top of that, the slightly strengthened NitrRR performance of Ni–Ru ball-flower structure compared with the mechanical mix of Ru and Ni show that nanometer range electronic interactions play a supportive role (Figures S30–S32): the Ni stamen and Ru petals here integrate to a coupled dyadic system (Figures 3d–f, S33a and S34). As indicated in Figure 3g, lattice distortions are observed at the interface of Ru and

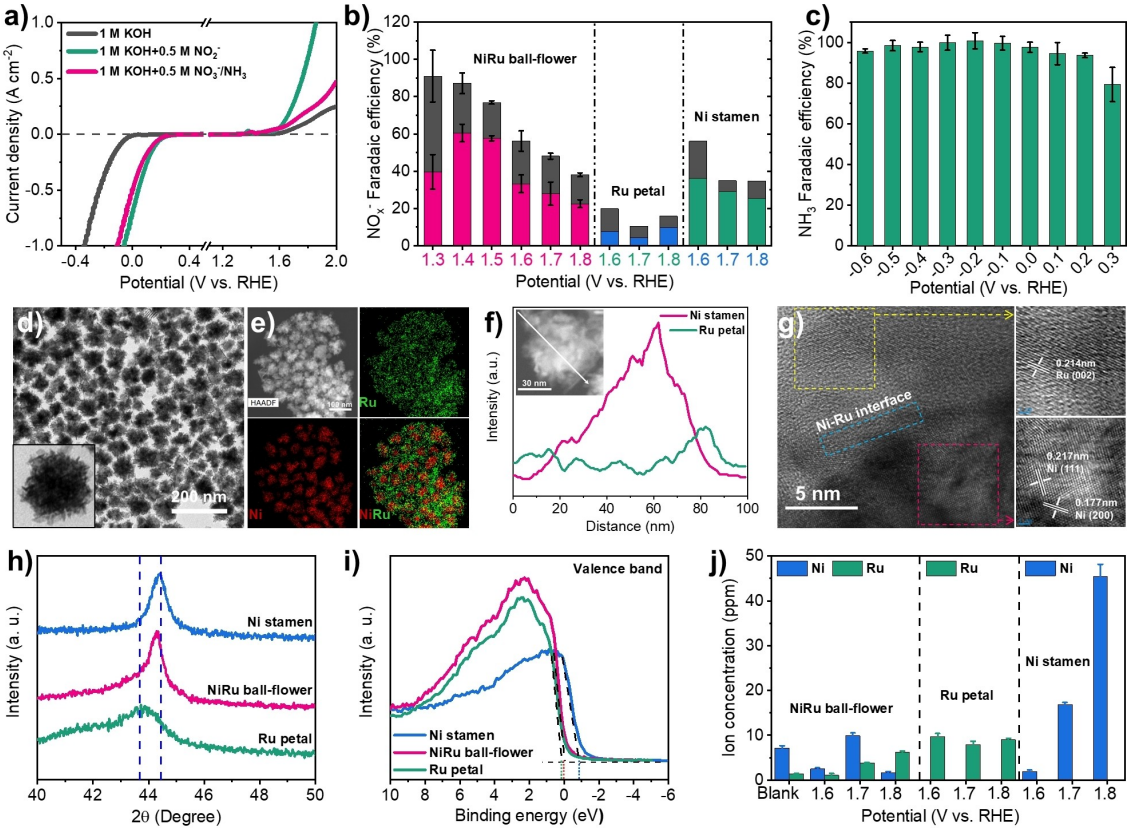

Figure 3. Performance evaluations of electrochemical nitrogen cycle between NH_3 and NO_x^- ($x=2$, 3) and structure characterization of catalysts. a) Linear sweep voltammetry curves of NiRu ball-flower Janus electrocatalysts recorded in various electrolytes show that the nitrogen cycle between NH_3 and NO_x^- is possibly achieved. LSV curves were recorded with automatic *iR* compensation by electrochemical workstation. b) Faradaic efficiency for NO_x^- ($x=2$, 3) synthesis by NH_3 oxidation reaction (AOR) at the applied potential of 1.3 V to 1.8 V vs. RHE (Pink, blue, and green: NO_2^- Faradaic efficiency. Brown: NO_3^- Faradaic efficiency). c) Faradaic efficiency for NH_3 synthesis by NO_3^- reduction reaction (NitrRR) from the potential of −0.6 V to +0.3 V vs. RHE. d) TEM images of NiRu ball-flower structure (Inset of (d) is enlargement image). e) STEM and elemental mapping images of NiRu ball-flower sample. f) STEM image and the white line arrow corresponding to the line scan for elemental analysis. g) High-resolution TEM images of NiRu ball-flower nanoparticles. h) XRD patterns of three catalysts. i) Valence electronic signal of three catalysts obtained from XPS measurements. j) Ni and Ru ions concentration in electrolytes detected by ICP after 2-hour AOR for NiRu ball-flower catalyst.

Ni, which indicates the tight junction between the two metals. The results differ from those from the single components or the physical mixture of Ni and Ru, which all show incomplete eight-electron transformation and poor structural stability (Figures S35–S40). High-resolution transmission electron microscopy (TEM) image of NiRu catalyst also shows the interplanar spacing of the Ni (111) plane increases from 0.200 nm or 0.201 nm in pure Ni particles (Figure S37) to 0.217 nm in NiRu catalyst. This enhanced interplanar spacing agrees with the results of X-ray diffraction (XRD) and reflects the hybridization between the Ni and Ru components (Figure 3h).

The electronic interaction between Ni and Ru elements was also followed by X-ray photoelectron spectroscopic (Figure S41). The valence band maximum value and the binding energy of Ni 2p in the mixed metallic NiRu catalyst is close to that of the Ru sample and positive-shifted relative to Ni sample (Figures 3i and S41b). This fits well with the results presented above. It confirms the well-defined generation of charge transfer at the interface between Ni and Ru, as indicated by the fact that the negative peaks (charge depletion) are on the Ru side and the positive peaks (charge accumulation) are on the Ni side from the differential charge density of NiRu structure by the density-functional theory (DFT) computations (Figure S42). Such strong electronic exchange interactions improve the structural and performance stability during electrochemical cycling (Figures S39–S45). For instance, Ni and Ru ions stay almost undetectable in the electrolyte by inductively coupled plasma-mass spectrometry (ICP) when using the NiRu catalyst for two-hour AOR, while approximately 45 ppm of dissolved Ni ions were found for the pure Ni catalyst (Figures 3j and S44, S45). These results indicate that the charge transfer from Ru to Ni inhibits nucleophilic ammonia corrosion.

To further investigate the catalytic mechanism of NiRu Janus electrocatalyst, the electrocatalytic performances of pure Ru catalyst and Ni catalyst for NO_3^- reduction and NH_3 oxidation reactions were studied. Based on the poor activity of the Ru catalyst compared to the Ni catalyst, the AOR performance of the NiRu Janus electrocatalyst is mainly derived from the Ni stamen (Figures 3b and S46). In addition, the excellent NitrRR performance mainly originated from the Ru petals in the optimized NiRu catalyst (Figures S47–S51), which can be well illustrated by the inferior or similar performances using pure Ni catalyst and Ru catalyst, respectively, under otherwise unchanged experimental conditions (Figures S47 and S52). Therefore, in the NiRu Janus electrocatalyst, the different roles of Ni stamen and Ru petals promoted outstanding catalytic activity towards the AOR and NitrRR, respectively.

In conclusion, a biomimetic, eight-electron nitrogen cycle was presented as a promising cathode chemistry for the future storage and release of renewable electricity. The concept of the reversible eight-electron conversion between NO_3^- and NH_3 was realized with an overall efficiency of up to 91 %, based on novel NiRu ball-flower Janus electrocatalyst. The redox couple of NO_3^-/NH_3 was then coupled with the Zn metal anode to construct a hybrid Zn–N RFB ($Zn–Zn^{2+}//NO_3^-–NH_3$ RFB), in which the transformation between NO_3^- and NH_3 delivered a capacity contribution of around 93 %. This hybrid flow battery results in a record high practical energy density of 577 $Wh\,L^{-1}$, making it stand out from previously reported battery systems. The current experimental set-up realizes already 66.2 % of the theoretical capacity, and the differences can be mostly related to the lower cell voltage, which might be caused by the catalytic overpotentials, but is mainly related to inner electric resistances and impedances of our non-optimized demonstrator cell. In addition, if NO_3^- is not completely converted to NH_3 with eight-electron transfer during the discharging process, the presence of NO_2^- intermediates could also lead to a loss of energy in the hybrid flow battery.

Importantly, the constructed Zn–N RFB continuously worked for at least 930 charging-discharging cycles (12.9 days), indicating the broad prospects for practical application. We also believe that the performance of the flow battery could be further enhanced by optimizing the setup design, exploiting more efficient electrocatalysts to elevate the eight-electron reaction path, developing tailor-made alkaline separation membranes, and coupling more appropriate anode redox reactions to enlarge the operating voltage. This is the scope of ongoing investigations.

Acknowledgements

The authors express their gratitude to the financial supports by the National Key R&D Program of China (Grant No. 2022YFB4002602), the Natural Science Foundation of China (22138005) and National Postdoctoral Program for Innovative Talents (BX20190119). This work has been supported by the New Cornerstone Science Foundation through the XPLORER PRIZE. M.A. and G.F.C. like to thank the Max Planck Society for continued support. Open Access funding enabled and organized by Projekt DEAL.

Conflict of Interest

The authors declare no conflict of interest.

Data Availability Statement

The data that support the finding of this study are available from the corresponding author upon reasonable request.

Keywords: Nitrate reduction · Ammonia oxidation · Eight-electron energy storage · Zinc-nitrogen battery · NiRu Janus catalyst

[1] T. Janoschka, N. Martin, U. Martin, C. Friebe, S. Morgenstern, H. Hiller, M. D. Hager, U. S. Schubert, *Nature* **2015**, *527*, 78–81.

[2] a) R. Feng, X. Zhang, V. Murugesan, A. Hollas, Y. Chen, Y. Shao, E. Walter, N. P. N. Wellala, L. Yan, K. M. Rosso, W. Wang, *Science* **2021**, *372*, 836–840; b) G. L. Soloveichik, *Chem.*

Rev. **2015**, *115*, 11533–11558; c) M. Park, J. Ryu, W. Wang, J. Cho, *Nat. Rev. Mater.* **2017**, *2*, 16080.
[3] a) J. Winsberg, T. Janoschka, S. Morgenstern, T. Hagemann, S. Muench, G. Hauffman, J.-F. Gohy, M. D. Hager, U. S. Schubert, *Adv. Mater.* **2016**, *28*, 2238–2243; b) C. Sun, X. Shi, Y. Zhang, J. Liang, J. Qu, C. Lai, *ACS Nano* **2020**, *14*, 1176–1184.
[4] a) C. Xie, Y. Liu, W. Lu, H. Zhang, X. Li, *Energy Environ. Sci.* **2019**, *12*, 1834–1839; b) B. Huskinson, M. P. Marshak, C. Suh, S. Er, M. R. Gerhardt, C. J. Galvin, X. Chen, A. Aspuru-Guzik, R. G. Gordon, M. J. Aziz, *Nature* **2014**, *505*, 195–198.
[5] A. Khor, P. Leung, M. R. Mohamed, C. Flox, Q. Xu, L. An, R. G. A. Wills, J. R. Morante, A. A. Shah, *Mater. Today Energy* **2018**, *8*, 80–108.
[6] B. Li, Z. Nie, M. Vijayakumar, G. Li, J. Liu, V. Sprenkle, W. Wang, *Nat. Commun.* **2015**, *6*, 6303.
[7] a) S. Hou, L. Chen, X. Fan, X. Fan, X. Ji, B. Wang, C. Cui, J. Chen, C. Yang, W. Wang, C. Li, C. Wang, *Nat. Commun.* **2022**, *13*, 1281; b) K. Peng, Y. Li, G. Tang, Y. Liu, Z. Yang, T. Xu, *Energy Environ. Sci.* **2023**, *16*, 430–437.
[8] a) C. Wang, X. Li, X. Xi, W. Zhou, Q. Lai, H. Zhang, *Nano Energy* **2016**, *21*, 217–227; b) Z. Yuan, Y. Duan, T. Liu, H. Zhang, X. Li, *iScience* **2018**, *3*, 40–49; c) C. Xie, Y. Duan, W. Xu, H. Zhang, X. Li, *Angew. Chem. Int. Ed.* **2017**, *56*, 14953–14957; d) C. Xie, H. Zhang, W. Xu, W. Wang, X. Li, *Angew. Chem. Int. Ed.* **2018**, *57*, 11171–11176; e) Y. Cheng, N. Zhang, Q. Wang, Y. Guo, S. Tao, Z. Liao, P. Jiang, Z. Xiang, *Nano Energy* **2019**, *63*, 103822; f) L. Xia, T. Long, W. Li, F. Zhong, M. Ding, Y. Long, Z. Xu, Y. Lei, Y. Guan, D. Yuan, Y. Zhang, C. Jia, L. Sun, Q. Sun, *Small* **2020**, *16*, 2003321; g) J. O. G. Posada, A. J. R. Rennie, S. P. Villar, V. L. Martins, J. Marinaccio, A. Barnes, C. F. Glover, D. A. Worsley, P. J. Hall, *Renewable Sustainable Energy Rev.* **2017**, *68*, 1174–1182.
[9] a) S. S. Shinde, C. H. Lee, J.-Y. Jung, N. K. Wagh, S.-H. Kim, D.-H. Kim, C. Lin, S. U. Lee, J.-H. Lee, *Energy Environ. Sci.* **2019**, *12*, 727–738; b) L. Zhang, P. Lu, Y. Luo, J. Y. Zheng, W. Ma, L.-X. Ding, H. Wang, *J. Mater. Chem. A* **2021**, *9*, 9609–9615; c) W. Sun, F. Wang, B. Zhang, M. Zhang, V. Küpers, X. Ji, C. Theile, P. Bieker, K. Xu, C. Wang, M. Winter, *Science* **2021**, *371*, 46–51.
[10] Z. Yuan, Y. Yin, C. Xie, H. Zhang, Y. Yao, X. Li, *Adv. Mater.* **2019**, *31*, 1902025.
[11] Y. V. Tolmachev, A. Piatkivskyi, V. V. Ryzhov, D. V. Konev, M. A. Vorotyntsev, *J. Solid State Electrochem.* **2015**, *19*, 2711–2722.
[12] S. G. Bratsch, *J. Phys. Chem. Ref. Data* **1989**, *18*, 1–21.
[13] S. Garcia-Segura, M. Lanzarini-Lopes, K. Hristovski, P. Westerhoff, *Appl. Catal. B* **2018**, *236*, 546–568.
[14] a) A. Stirling, I. Pápai, J. Mink, D. R. Salahub, *J. Chem. Phys.* **1994**, *100*, 2910–2923; b) R. Hawtof, S. Ghosh, E. Guarr, C. Xu, R. Mohan Sankaran, J. N. Renner, *Sci. Adv.* **2019**, *5*, eaat5778; c) X. Yang, S. Mukherjee, T. O'Carroll, Y. Hou, M. R. Singh, J. A. Gauthier, G. Wu, *Angew. Chem. Int. Ed.* **2023**, *62*, e202215938.
[15] a) Y. Guo, R. Zhang, S. Zhang, Y. Zhao, Q. Yang, Z. Huang, B. Dong, C. Zhi, *Energy Environ. Sci.* **2021**, *14*, 3938–3944; b) H. Jiang, G. Chen, O. Savateev, J. Xue, L. X. Ding, Z. Liang, M. Antonietti, H. Wang, *Angew. Chem. Int. Ed.* **2023**, *62*, e202218717.
[16] a) J. G. Chen, R. M. Crooks, L. C. Seefeldt, K. L. Bren, R. M. Bullock, M. Y. Darensbourg, P. L. Holland, B. Hoffman, M. J. Janik, A. K. Jones, M. G. Kanatzidis, P. King, K. M. Lancaster, S. V. Lymar, P. Pfromm, W. F. Schneider, R. R. Schrock, *Science* **2018**, *360*, eaar6611; b) D. R. MacFarlane, P. V. Cherepanov, J. Choi, B. H. R. Suryanto, R. Y. Hodgetts, J. M. Bakker, F. M. Ferrero Vallana, A. N. Simonov, *Joule* **2020**, *4*, 1186–1205; c) C. H. Christensen, T. Johannessen, R. Z. Sørensen, J. K. Nørskov, *Catal. Today* **2006**, *111*, 140–144; d) O. Elishav, B. Mosevitzky Lis, E. M. Miller, D. J. Arent, A. Valera-Medina, A. Grinberg Dana, G. E. Shter, G. S. Grader, *Chem. Rev.* **2020**, *120*, 5352–5436; e) H. Jiang, G.-F. Chen, O. Savateev, H. Wang, *Joule* **2023**, *7*, 253–256.
[17] a) C. A. Grande, K. A. Andreassen, J. H. Cavka, D. Waller, O.-A. Lorentsen, H. Øien, H.-J. Zander, S. Poulston, S. García, D. Modeshia, *Ind. Eng. Chem. Res.* **2018**, *57*, 10180–10186; b) H.-Y. Liu, H. M. C. Lant, J. L. Troiano, G. Hu, B. Q. Mercado, R. H. Crabtree, G. W. Brudvig, *J. Am. Chem. Soc.* **2022**, *144*, 8449–8453; c) S. Han, C. Wang, Y. Wang, Y. Yu, B. Zhang, *Angew. Chem. Int. Ed.* **2021**, *60*, 4474–4478.
[18] a) J. Li, G. M. Zhan, J. H. Yang, F. J. Quan, C. L. Mao, Y. Liu, B. Wang, F. C. Lei, L. J. Li, A. W. M. Chan, L. P. Xu, Y. B. Shi, Y. Du, W. C. Hao, P. K. Wong, J. F. Wang, S. X. Dou, L. Z. Zhang, J. C. Yu, *J. Am. Chem. Soc.* **2020**, *142*, 7036–7046; b) G.-F. Chen, Y. Yuan, H. Jiang, S.-Y. Ren, L.-X. Ding, L. Ma, T. Wu, J. Lu, H. Wang, *Nat. Energy* **2020**, *5*, 605–613; c) Y. Wang, A. Xu, Z. Wang, L. Huang, J. Li, F. Li, J. Wicks, M. Luo, D. H. Nam, C. S. Tan, Y. Ding, J. Wu, Y. Lum, C. T. Dinh, D. Sinton, G. Zheng, E. H. Sargent, *J. Am. Chem. Soc.* **2020**, *142*, 5702–5708; d) F.-Y. Chen, Z.-Y. Wu, S. Gupta, D. J. Rivera, S. V. Lambeets, S. Pecaut, J. Y. T. Kim, P. Zhu, Y. Z. Finfrock, D. M. Meira, G. King, G. Gao, W. Xu, D. A. Cullen, H. Zhou, Y. Han, D. E. Perea, C. L. Muhich, H. Wang, *Nat. Nanotechnol.* **2022**, *17*, 759–767.
[19] a) K. A. Stoerzinger, R. R. Rao, X. R. Wang, W. T. Hong, C. M. Rouleau, Y. Shao-Horn, *Chem* **2017**, *2*, 668–675; b) M. Görlin, J. Ferreira de Araujo, H. Schmies, D. Bernsmeier, S. Dresp, M. Gliech, Z. Jusys, P. Chernev, R. Kraehnert, H. Dau, P. Strasser, *J. Am. Chem. Soc.* **2017**, *139*, 2070–2082; c) O. Diaz-Morales, D. Ferrus-Suspedra, M. T. M. Koper, *Chem. Sci.* **2016**, *7*, 2639–2645.
[20] E. Sánchez-Díez, E. Ventosa, M. Guarnieri, A. Trovò, C. Flox, R. Marcilla, F. Soavi, P. Mazur, E. Aranzabe, R. Ferret, *J. Power Sources* **2021**, *481*, 228804.
[21] Y. Huang, H. Yang, T. Xiong, D. Adekoya, W. Qiu, Z. Wang, S. Zhang, M. S. Balogun, *Energy Storage Mater.* **2020**, *25*, 41–51.
[22] a) R. Zhang, Y. Guo, S. Zhang, D. Chen, Y. Zhao, Z. Huang, L. Ma, P. Li, Q. Yang, G. Liang, C. Zhi, *Adv. Energy Mater.* **2022**, *12*, 2103872; b) Z. Li, Z. Deng, L. Ouyang, X. Fan, L. Zhang, S. Sun, Q. Liu, A. A. Alshehri, Y. Luo, Q. Kong, X. Sun, *Nano Res.* **2022**, *15*, 8914–8921; c) Q. Liu, L. Xie, J. Liang, Y. Ren, Y. Wang, L. Zhang, L. Yue, T. Li, Y. Luo, N. Li, B. Tang, Y. Liu, S. Gao, A. A. Alshehri, I. Shakir, P. O. Agboola, Q. Kong, Q. Wang, D. Ma, X. Sun, *Small* **2022**, *18*, 2106961.
[23] Z.-Y. Wu, M. Karamad, X. Yong, Q. Huang, D. A. Cullen, P. Zhu, C. Xia, Q. Xiao, M. Shakouri, F.-Y. Chen, J. Y. Kim, Y. Xia, K. Heck, Y. Hu, M. S. Wong, Q. Li, I. Gates, S. Siahrostami, H. Wang, *Nat. Commun.* **2021**, *12*, 2807.
[24] a) Y. Huang, L. Hu, R. Liu, Y. Hu, T. Xiong, W. Qiu, M. S. Balogun, A. Pan, Y. Tong, *Appl. Catal. B* **2019**, *251*, 181–194; b) H. Zhang, C. Wang, H. Luo, J. Chen, M. Kuang, J. Yang, *Angew. Chem. Int. Ed.* **2023**, *62*, e202217071.

Manuscript received: April 24, 2023
Accepted manuscript online: May 26, 2023
Version of record online: June 20, 2023